CHAPTER 3.3

# Visualizing TPP structures with coherent Raman scattering microscopy

**Richard Prince[a], Peixun Fan[b], Yongfeng Lu[b], Tommaso Baldacchini[c], Eric O. Potma[a,d]**

[a]Department of Biomedical Engineering, University of California, Irvine, CA, United States
[b]Department of Electrical Engineering, University of Nebraska, Lincoln, NE, United States
[c]Schmid College of Science and Technology, Chapman University, Orange, CA, United States
[d]Department of Chemistry, University of California, Irvine, CA, United States

## 1 Introduction

The chemical and physical processes that take place in the sub-$\mu m^3$ volume of a tightly focused laser beam during TPP writing are complex. Variations in photon flux, exposure time, heat dissipation kinetics, and concentration of photoinitiator and monomer can give rise to differences in the properties of the polymer material, such as the degree of conversion, density, and mechanical properties. Quality control of the TPP process, especially in terms of the chemical conversion during and immediately after laser illumination, is highly desirable. Alongside developments in TPP writing techniques, the detailed chemical in situ characterization of TPP structures plays an equally important role in driving the technology toward maturation [1].

Direct inspection of the chemical properties of TPP structures can be challenging. Many analytical techniques, such as mass spectroscopy, differential scanning calorimetry, or conventional optical spectroscopy, are either destructive or incompatible with in situ characterization. The particular environment of the TPP process stipulates that the polymerized material can be examined on an optical microscopy platform, which offers limited physical space for the incorporation of additional analytical instruments. Fortunately, the optical microscope itself offers several intrinsic analytical capabilities, such as simple visual inspection, phase contrast microscopy, and laser scattering measurements, which can be helpful for interrogating the morphology and density of the polymerized material. Yet, measurements of this nature do not provide chemical information. To access chemical properties, optical spectroscopy, and in particular vibrational microspectroscopy, can be integrated into the platform used for TPP fabrication.

Vibrational spectroscopy uses light to probe molecular vibrational resonances in the material. These motions correspond to localized chemical bond vibrations or vibrational motions that include the coupled motions of several bonds. The chemical bond and chemical group sensitivity make vibrational spectroscopy an ideal probe for chemical

*Three-Dimensional Microfabrication Using Two-Photon Polymerization*
https://doi.org/10.1016/B978-0-12-817827-0.00055-2

changes in the sample. An added benefit is that no extrinsic labels are needed to access this information, as the contrast is derived directly from the material of interest itself.

Molecular vibrational modes have resonance frequencies in the 3–100 THz range. These modes can be driven in a resonant fashion when light is supplied in the same frequency range, corresponding to wavelengths of ~4 to 100 μm, in the infrared (IR) range of the electromagnetic spectrum. Resonant excitation results in an energy exchange between the light and the material, which can be detected as wavelength-dependent absorption losses on a spectrometer. A routine method for chemical analysis, IR absorption spectroscopy has also been used to measure the curing of the degree of conversion in polymer resins [2]. The technique can also be incorporated in a microscope configuration. Nonetheless, it is not trivial to use IR light in the microscope system optimized for TPP fabrication. The high NA lenses used in TPP fabrication are opaque to IR radiation, and many other optical components are incompatible for use with IR light. For this reason, chemical analysis of TPP structures with IR absorption spectroscopy is not a natural choice.

Raman spectroscopy offers an attractive alternative. This technique is based on an off-resonant, inelastic scattering effect, which makes it possible to probe molecular vibrations with visible laser light. In Raman spectroscopy, a narrow band laser beam is used to illuminate the sample and scattered light is collected and dispersed onto a spectrometer. The Raman effect gives rise to scattered light contributions at red-shifted wavelengths, and the observed frequency shifts correspond to the vibrational frequencies of the molecular modes. Because visible or near-infrared light can be used, probing Raman scattered light is relatively straightforward in the optical microscope system used in TPP fabrication. Raman microspectroscopy has been successfully used for examining chemical details of TPP structures in situ [3–5].

Despite the usefulness of Raman microspectroscopy for chemical analysis, the technique offers limited time resolution [6]. The Raman effect is weak, and in order to accumulate a Raman spectrum of sufficient quality, pixel dwell times of 0.1–10 s are needed. Such relatively long signal integration times are incompatible with rapid mapping of TPP structures. Since fast mapping is as important as fast writing, regular Raman microspectroscopy may have limited utility in practical quality control of the TPP process.

Faster versions of the Raman microscopy technique are available. Coherent Raman scattering (CRS) microscopy, a nonlinear version of Raman microscopy, offers pixel dwell times many orders of magnitude shorter than conventional Raman [7–9]. In CRS, the sample is illuminated with laser light of different frequencies, such that the difference frequency of the incident laser beams corresponds to the frequency of a Raman active mode in the sample. Under these conditions, molecular vibrational modes can be driven in unison, producing a strong optical response. CRS microscopy methods have been successfully used for rapid mapping of biological samples, producing chemically selective images with pixel dwell times of less than a microsecond.

Beyond biological applications, CRS microscopy also has attractive imaging properties for inspection of TPP structures [1, 10, 11]. In this chapter, we discuss the principles of CRS microscopy and its promising applications to analyzing TPP microstructures. We first provide a brief description of the Raman effect and how CRS can be used to increase the yield of the Raman-derived signal. Next, we discuss the basics of the CRS microscope and its integration with TPP microfabrication instruments. We highlight several applications of CRS mapping of TPP structures, as well as show several examples in which information about the degree of conversion can be obtained from CRS measurements. Finally, we offer some prospects of the CRS technique in the context of characterizing materials fabricated by the TPP technique.

## 2 Basics of coherent Raman scattering microscopy

### 2.1 Nature of the Raman interaction

The Raman effect provides information about atomic displacements in a chemical structure. The motion of atoms relative to one another in a structure is sometimes referred to as a nuclear mode. For instance, the periodic modulation of the distance of the carbon and hydrogen atom in a C—H bond qualifies as a nuclear mode. In this case, the on-axis modulation of the interatomic distance is called a stretching vibration. There are different kinds of nuclear modes, including the symmetric and asymmetric stretching vibrations, bending vibrations, torsional motions, and combinations of such motions. More generally, the set of all possible motions of atoms in a chemical structure that are allowed by symmetry forms a set of normal modes. A (nonlinear) chemical structure of N atoms has a total of 3N-6 vibrational normal modes. The Raman effect can probe a subset of these normal modes, namely, those modes that are Raman-active.

We can think of any normal mode as an oscillatory motion along a general nuclear coordinate $Q$. A vibrational mode can then be modeled as a time-harmonic motion along $Q$:

$$Q(t) = 2Q_0 \cos \omega_\nu t$$

Here $Q_0$ is the amplitude of the motion, and $\omega_\nu$ is the frequency of the nuclear mode. What is special about the Raman effect is that it can probe nuclear degrees of freedom through the motions of electrons. At first sight, this is rather remarkable. Since vibrational normal modes have resonance frequencies $\omega_\nu$ that are much lower than the frequencies $\omega$ of the visible or near-infrared excitation light, the incident radiation is unable to resonantly drive the nuclear motions. The nuclei are too "slow" to follow the rapid oscillations of the electromagnetic field. However, the electrons, which are much lighter, can follow the electric field oscillations. Consequently, upon illumination, the atomic nuclei in the structure are surrounded by an electron bath that is rapidly moving along with the driving field. The magnitude of the electron motions is indicated by the electronic

polarizability $\alpha$; the higher $\alpha$, the easier it is to set the electrons in motion with the light field. If there is any coupling between the electron motion and the nuclear motion, then some of the motional energy of the electrons can be transferred to the nuclear modes. Mathematically, we can describe such a coupling by the term $\delta\alpha/\delta Q$, which is nonzero if a small change in the electron polarizability ($\delta\alpha$) leads to a small change in the nuclear motion ($\delta Q$), or vice versa. We can then write the electronic polarizability as a Taylor series expansion along $Q$ [12]:

$$\alpha(t) = \alpha_0 + \left(\frac{\delta\alpha}{\delta Q}\right)_0 Q(t) + \cdots$$

where $\alpha_0$ is the purely electronic contribution and the second term indicates the electronic motion that is affected by the presence of the nuclear mode. The Raman effect probes the electron motions represented by the second term. The presence of the nuclear mode shifts the oscillation frequency $\omega$ of the electrons with the nuclear vibrational energy $\omega_\nu$, giving rise to electron motions at frequencies ($\omega \pm \omega_\nu$). This results in scattered light contributions at new frequencies. By measuring the frequency shift of the Raman scattered light, we can thus determine the frequencies of Raman active normal modes of the chemical structure, see Fig. 3.3.1A.

The $\delta\alpha/\delta Q$ term plays an important role in Raman spectroscopy. The larger this coupling term between electronic and nuclear degrees of freedom, the stronger the Raman scattered signal. The magnitude of this term depends on the symmetry of the normal mode. Consequently, it is related to the selection rule of Raman spectroscopy, which states that a mode is Raman active if the polarizability changes as a consequence of the vibration. In general, the change in electronic polarizability due to the vibration is

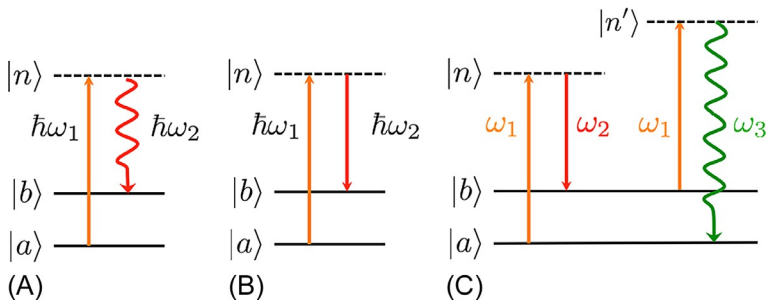


**Fig. 3.3.1** Jablonski diagrams for spontaneous Raman scattering (A), stimulated Raman scattering (B) and coherent anti-Stokes Raman scattering (C). Here molecular ground state is indicated by $|a>$ and the vibrationally excited state is denoted as $|b>$. The $|n>$ states are so-called virtual states, states that are not supported by the molecule and in which the system can only reside for a very short time. A curved downward arrow indicates a spontaneously emitted photon, a straight downward arrow indicates a stimulated emitted photon. Both spontaneous Raman and stimulated Raman scattering are two-photon processes, whereas CARS is a four-photon process.

larger in chemical groups that have more isotropic electron distributions, relative to groups that have a more anisotropic distribution of electrons. In practice, many modes in organic molecules display Raman activity, making Raman spectroscopy and excellent method for examining chemical content and structure.

## 2.2 The coherent Raman scattering signal

The major drawback of the Raman technique is its weakness. The Raman cross sections of molecular modes are small, of the order of $10^{-28}$ cm$^2$ for some of the strongest Raman scatterers. For comparison, the cross section for electronic absorption of a dye molecule is $\sim 10^{-16}$ cm$^2$, and the cross section of resonant IR excitation of vibrational modes is $\sim 10^{-18}$ cm$^2$. This implies that, in terms of the molecular response, Raman-type excitation of a vibrational mode is about 10 orders of magnitude less efficient than a direct IR excitation of a vibrational mode. Although Raman offers many advantages over IR absorption spectroscopy, the strength of the molecular response is not one of them.

The weakness of the Raman effect stipulates that it takes time to accumulate a signal of sufficient signal to noise. Using the sub-μm$^3$ focal volume of a high NA microscope objective as the probing spot, it is not practical to acquire a quality Raman spectrum from TPP structures in less than 100 ms. Using more pump power is an option, but photodamaging effects put a limit on how much laser power can be used.

CRS provides a route to increasing the signal yield derived from the Raman process. The key difference between CRS and spontaneous Raman scattering is that the vibrational oscillators are driven into motion by two laser field interactions. These two fields lock the vibrational motions into phase, resulting in the synchronous vibration of Raman scatterers in the interaction volume. This is different from the case of spontaneous Raman scattering, where the vibrational phase of the molecules in focus are random relative to one another, even though a (single) *coherent* laser beam was used to excite them. Phase synchronization means that the radiation that follows from driven molecules is also in phase, giving rise to a strong signal in the direction where the radiation constructively interferes, the so-called phase-matched direction. This signal can be up to $10^5$ times as high as the spontaneous Raman signal, using approximately the same average excitation power and the same microscopic probing volume.

To achieve the phase synchronized excitation of molecular oscillators, CRS uses two fields, called pump and Stokes fields, of frequency $\omega_p$ and $\omega_S$, respectively. The vibrational mode is driven by the difference frequency $\Omega = \omega_p - \omega_S$, and the molecular response grows strongest when $\Omega$ matches the vibrational mode frequency $\omega_\nu$. The modulation at $\Omega$ in the sample can be detected as sidebands of the incident frequencies. There are a total of four different frequencies, or sideband, at which the coherent Raman scattering signal can be detected, namely, $\omega_p \pm \Omega$ and $\omega_S \pm \Omega$. The most common strategy is to detect the signal at $\omega_p + \Omega$, which is called the coherent anti-Stokes Raman scattering

(CARS) signal, or at $\omega_S + \Omega = \omega_p$, which is called the stimulated Raman scattering loss (SRL) signal. The Jablonski diagrams for SRL and CARS are shown in Fig. 3.3.1B and C, respectively. Although both signals report on exactly the same coherently driven molecular vibration, and therefore reveal the same molecular information, there are some differences between the CARS and SRL signals.

The CARS signal appears at a color different from the incident laser fields. It can be isolated rather easily with a spectral bandpass filter and thus detected with a very high efficiency using a standard photomultiplier tube (PMT) on the microscope system. The signal is, however, accompanied by the so-called nonresonant background. These are signal contributions at $\omega_p + \Omega$ that are purely electronic in nature and do not involve the nuclear vibration. Because the electronic contribution is coherently mixed with the vibrationally resonant contribution, it is nontrivial to remove this nonresonant background. This is sometimes seen as a significant limitation of CARS, especially in cases when the electronic contribution overwhelms the vibrational signal. For the visualization of TPP structures, the electronic background is manageable, and even weak fingerprint vibrations can be observed without significant difficulty [11].

The SRL signal is detected at the color of the pump beam. The signal appears as a loss signal on the incident pump laser beam [13]. A sensitive PMT is in this case not a good detector, as the photodetector needs to be able to discriminate small changes on a large laser background. For this purpose, a simple silicon photodiode can be implemented, which has an excellent dynamic range. To separate the SRL signal from the laser background, a modulation scheme can be used, whereby the Stokes beam is amplitude-modulated and the SRL-mediated modulation transfer to the pump beam is registered. Electronic demodulation of the pump signal then yields the magnitude of the SRL signal [14–16]. Although this detection scheme is more complicated than in CARS, the added benefit is that the SRL signal is devoid of the nonresonant background. In addition, the SRL signal displays a linear dependence on the number of Raman scatterers in the focal volume, which makes the SRL response easier to interpret than the CARS signal (which has a nonlinear concentration dependence). The SRL spectrum is directly proportional to the Raman spectrum, enabling a straightforward spectroscopic analysis. Both CARS and SRL can be integrated on the same microscope, and they are typically registered simultaneously.

## 2.3 Chemical sensitivity

Since both CARS and SRL depend on the spectroscopic information provided by the Raman spectrum, it is relevant to examine what kind of information can be gleaned from CRS microscopic measurements of TPP structures. Fig. 3.3.2 shows the Raman spectrum of a resin before and after photoinduced polymerization. The resin consists of the photoinitiator Irgacure 369 and two acrylic monomers (SR499 and SR368). The

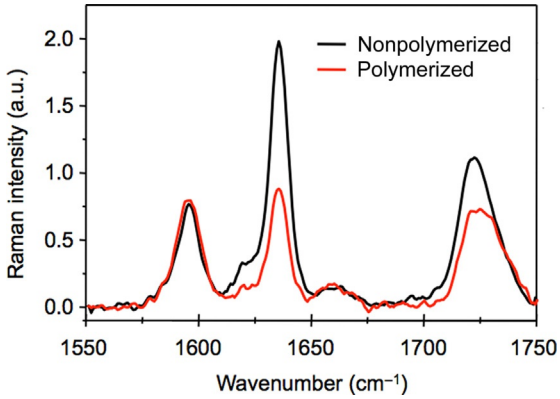


**Fig. 3.3.2** Raman spectroscopy of polymerized and nonpolymerized acrylic photoresist. Raman spectra were taken in a Raman microscope. Sample was a thin film on glass before *(black)* and after *(red)* UV illumination.

fingerprint region shown contains several important vibrational modes. The 1595 $cm^{-1}$ mode can be attributed to one of the aromatic ring vibrations of the photoinitiator. Since the aromatic ring itself is not involved in the photochemistry, we do not expect a change in the magnitude of this mode before and after polymerization. The 1635 $cm^{-1}$ peak is assigned to the carbon-carbon double bond of the acrylic polymer. The number of these double bonds is depleted during polymerization, so we expect that the strength of this band will decrease after the photoreaction. This is indeed observed. The change in the 1635 $cm^{-1}$ peak strength is directly related to the degree of conversion.

A third significant signature peaks near 1720 $cm^{-1}$. This vibrational energy corresponds to the carbonyl stretching mode. We see that the magnitude of the vibration decreases and that the feature slightly shifts to higher vibrational energies. Since the number of carbonyl groups is conserved during polymerization, these observations cannot be attributed to a chemical change. Rather, the change reflects subtle changes in the local chemical environment of the carbonyl group [11]. After the polymer is formed, the adjacent C═C bond has been converted to a single bond, which breaks the π-bond electron delocalization with the carbonyl group. The loss of electron delocalization increases the localization of the carbonyl stretching vibrational mode, which generally leads to a loss of Raman scattering efficiency and a corresponding blue-shift.

This example shows that Raman spectroscopy can provide a rather in-depth account of the chemical changes that take place during polymerization. However, a correct reading of the Raman signatures is important. The signatures for different resins can differ markedly from the example discussed here. Additional care has to be taken to identify signatures of the photoinitiator, which sometimes overlap with vibrational lines of the monomer and polymer. Nonetheless, with the proper interpretation of the Raman spectral lines, the vibrational spectrum can provide a wealth of information

on the local polymer density and the degree of conversion, as well as identify unexpected chemical impurities in the material.

## 2.4 Resolution and concentration sensitivity limits

The resolution of the CRS microscope is comparable with the spatial resolution of a confocal microscope. The probing volume is defined by the overlap of the tightly focused pump and Stokes laser beams. The actual size depends on the wavelengths and microscope objective used. For a typical microscope objective with a numerical aperture of 1.0 or higher and NIR excitation beams, the lateral spatial resolution in CRS is of the order of 0.3 μm. Because CRS is a nonlinear process, the probing volume is confined in three dimensions, with an axial resolution that is commonly in the 1–2 μm range. This implies that CRS is capable of optical sectioning and that 3D reconstructions of TPP structures can be made based on a depth-resolved stack of CRS images.

The spatial resolution of CRS microscopy is not high enough to resolve features of the TPP structure that are beyond the diffraction limit. Although attempts have been made to adopt superresolution techniques in CRS microscopy, none of the current solutions represent a practical approach for examining TPP structures at a resolution beyond 0.3 μm when using NIR excitation light [17–19]. New developments that make use of excitation light at shorter wavelengths have shown promising results for high-resolution biological imaging well beyond 0.3 μm, and may have useful applications for TPP visualization as well.

The concentration sensitivity of CRS varies with the type of application. Assuming that the polymer structure is devoid of electronic resonances near the NIR excitation wavelengths, a typical detection limit is about $10^5$ vibrational oscillators within the focal volume. For instance, when tuning to a carbonyl stretching vibration, a TPP structure that fully overlaps with the focal probing volume must have a density of about a million carbonyl groups per fL, corresponding to a local concentration of about 2 mM. These conditions are fulfilled for typical TPP structures, implying that most TPP samples can be analyzed with CRS techniques. However, for progressively smaller features and lower density materials, the number of Raman scatterers (target chemical groups) may be too low and the CRS sensitivity may prove insufficient to produce a signal above the noise floor of the measurement.

# 3 The CRS microscope

The CRS microscope system consists of a laser light source, a laser scanner, a microscope frame, proper optics and detectors, and a computer equipped with image acquisition software. The most defining feature of the CRS system is the light source, which largely determines the type of CRS experiment that can be conducted. We will discuss the light source first, followed by a description of the imaging system.

## 3.1 Laser light source

CRS scales nonlinearly with the intensity of the incident light. Like other optical nonlinearities, the CRS process benefits from pulsed radiation over cw light. The magnitude of the CRS signal $S_{\mathrm{CRS}}$ scales as [20]:

$$S_{\mathrm{CRS}} \propto \frac{t}{(f\tau)^{n-1}} P^n$$

where $t$ is the pixel dwell time, $f$ is the laser repetition rate, $\tau$ is the pulse duration, and $P$ is the effective, average excitation power. The intensity scaling is indicated by the order $n$, where $n = 2$ for the SRL process and $n = 3$ for the CARS process. Keeping the average power ($P$) and pulse repetition rate ($f$) constant, the efficiency of CRS signal generation increases when the pulse duration is shortened. This implies that 100-fs pulses produce much stronger CRS signals than 10-ps pulses [21]. However, the temporal width and the spectral resolution are inversely related. By shortening the pulse, it becomes more difficult to resolve vibrational features. Since many Raman spectral signatures manifest themselves on the 10 $\mathrm{cm}^{-1}$ scale, a corresponding pulse duration of about 1 ps is preferred. For this reason, many CRS laser-scanning microscopes use narrow bandwidth, picosecond pulses. The use of picosecond pulses has the added benefit that the resonant-to-nonresonant signal ratio is much higher than that for femtosecond pulses [21].

Nonetheless, there are numerous alternative CRS excitation schemes that make use of broadband laser pulses. Examples include the combination of a picosecond and a femtosecond pulse, allowing excitation of many Raman modes simultaneously, which can subsequently be discriminated on a spectrometer [22, 23]. Another popular technique that uses femtosecond pulses is based on stretching the pulses in time, thus applying a spectral chirp, which can be used to "spectrally focus" the effective difference frequency [24, 25]. The spectral focusing technique makes it possible to perform CRS imaging experiments at a relatively high spectral resolution while using broadband pulses. Since femtosecond pulsed light is commonly used for the fabrication of TPP structures, the broadband CRS techniques may be particularly attractive, as it would enable imaging of TPP structures with a light source that is already part of the fabrication platform.

Besides the pulse width, another consideration is the repetition rate. The earlier equation suggests that the CRS signal increases when the pulse repetition rate is lowered while keeping the average power the same. Typical ultrafast laser oscillators have a repetition rate in the 50–100 MHz range. Keeping average powers below 10 mW in focus to avoid linear heating effects, pulse energies are commonly in the 100-pJ range. Lowering the repetition rate increases the signal yield, while increasing the pulse energy. Many structures, including TPP structures, experience photodamage as a consequence of nonlinear effects. Such effects can already be observed for pulses in the nJ range. This nonlinear photodamage puts a limit on the flexibility in tuning the repetition rate. In addition, when imaging directly in the resin, the peak power of the CRS imaging beams should

remain well below peak powers that induce TPP. In practice, the 100-MHz range has proven to be a good range for a wide host of CRS imaging applications [26].

An important requirement of CRS microscopy is the availability of laser light fields at the frequencies $\omega_p$ and $\omega_S$. In the case of narrowband excitation, this invariably means that two independent beams of different colors are needed. A typical narrowband CRS light source consists of a picosecond pump laser and an optical parametric oscillator to provide a second, spectrally adjustable light beam. Femtosecond CRS systems often use a main source and a single-pass frequency conversion step to generate a second beam. Some femtosecond sources provide such a wide bandwidth that both pump and Stokes frequencies are contained within the spectrum of a single pulse. In this chapter, we will discuss examples of both narrowband and broadband CRS light sources.

## 3.2 The imaging system

CRS microscopy can, with the proper modifications, be carried out on any standard inverted or upright optical microscope. Fast imaging requires a method for rapidly scanning the laser beam across the sample. For this purpose, a galvanometric scanner is the preferred choice. Some TPP fabrication platforms already have such a beam scanner incorporated. A scan lens and tube lens are used to map the beam angle onto the back aperture of a high NA microscope objective. The CRS signal is phase-matched in the forward direction, which implies that, for thin or transparent samples, the signal is strongest in the forward propagating direction. The signal is captured by a condenser lens, spectrally filtered, and subsequently sent to the photodetectors. We have seen that for CARS, detection is accomplished by a PMT, while for SRL a silicon photodiode is used instead. A rendering of a typical CRS imaging system is shown in Fig. 3.3.3.

## 3.3 Image acquisition

The pixel dwell times in narrowband CRS imaging applications vary between 100 ns to 200 μs. To visualize TPP samples, a pixel dwell time of 1–10 μs is typical. This results in a frame rate of about 1 frame/s for a 512 × 512 image, although faster image acquisition rates are possible. This frame rate allows a quick inspection of the TPP structure, and direct mapping of the structure during the writing process in situ. At average illumination powers in the 10-mW range, the pixel dwell times are too short to produce enough radicals for starting polymerization. Hence, under typical imaging CRS conditions, the visualization process does not alter the laser writing process [10].

The fastest CRS imaging studies are accomplished when the lasers are tuned to a single vibrational band at a given vibrational energy. The intensity of this band is then mapped, yielding an image that reports on the number density of a particular chemical group in the TPP structure. Such an image contains limited spectral information, as only a narrow range of the vibrational spectrum is used for generating contrast. The spectral

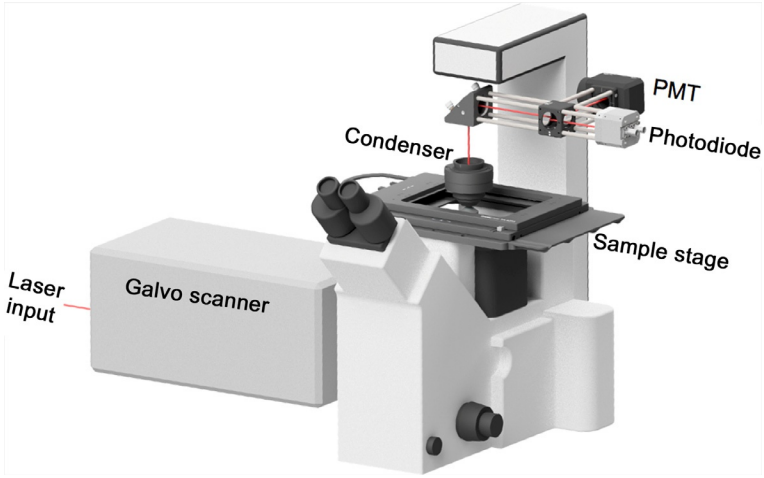


**Fig. 3.3.3** Basic layout of a laser-scanning CRS microscope. A galvanometric scanner is used to translate the laser focus rapidly in the sample plane. The CRS signals are commonly detected in the forward propagation direction, where they are captured by a condenser and sent to the photodetector. In CARS, a PMT is used whereas in SRS a photodiode is employed.

information can be expanded by recording sequential images at different vibrational energies. This produces a data cube ($x$, $y$, $\omega$), where every ($x$, $y$) pixel contains spectral depth ($\omega$). The data can subsequently be segmented using multivariate analysis or multicomponent computational methods. Naturally, recording of such a data cube extends the overall acquisition time. Whereas individual images can be acquired in less than a second, a typical spectral stack with 100 spectral points takes about a minute or so. Although this is much slower than rapid mapping based on a single Raman line, the information content is much higher. Several CRS schemes have been developed for accelerating the acquisition of hyperspectral data stacks [27].

Another form of data cube acquisition is three-dimensional mapping. Here ($x$, $y$) images are taken at different settings of $z$, thus producing a ($x$, $y$, $z$) data stack. Similar to the recording of hyperspectral data, 3D imaging extends the measurement time from several seconds to several minutes.

## 3.4 Combination with other modalities

The CRS modality is often combined with other microscopy modalities. It is relatively trivial to supplement the CRS channel with a transmission and reflection channel. These forms of contrast report on refractive index differences, which is often sufficient for obtaining a good impression of the micrometer scale morphology of the structure. The availability of pulsed laser light also offers the possibility of detecting additional optical nonlinearities, including third-harmonic generation (THG) and multiphoton excited fluorescence. THG is sensitive to interfaces and can provide additional information about

morphology. This technique has recently been used for the purpose of mapping TPP structures [28]. Fluorescence contrast is useful if the photoinitiator has a nonzero fluorescence quantum yield, in which case the distribution of the photoinitiator can be examined in the structure. Because both THG and multiphoton fluorescence are nonlinear techniques, they benefit from an intrinsic 3D resolution, enabling depth-resolved imaging of TPP structures.

## 4 Chemical mapping of 3D TPP microstructures

### 4.1 Material density mapping with C—H mode contrast

The most abundant chemical group in organic monomer and polymers used in TPP microfabrication is the carbon-hydrogen bond. This includes the $CH_2$ methylene unit and the $CH_3$ methyl groups. The carbon-hydrogen stretching vibrations can be found in the 2800–3000 $cm^{-1}$ range of the vibrational spectrum, where they often form overlapping band structures. Because of the abundance of these chemical groups, the corresponding band structure in this high-energy range is one of the strongest features of the Raman spectrum of TPP materials. Although C—H bonds are not involved in the polymerization reaction, their presence and strong signature can be used to map out TPP structures based on material density.

An example is shown in Fig. 3.3.4A, where TPP cubes are visualized with SRS microscopy. The signal is derived from vibrational modes in the 2800–3100 $cm^{-1}$ range.

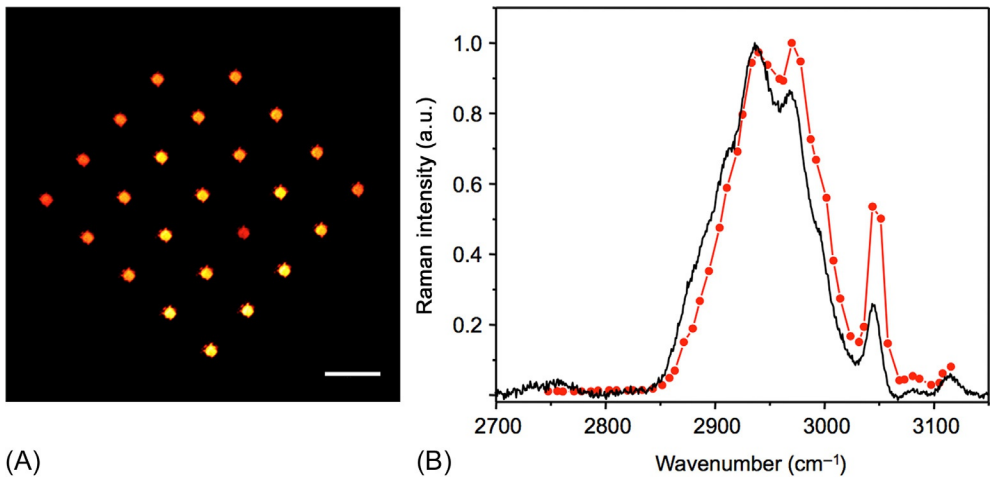


**Fig. 3.3.4** SRS density mapping. (A) Pattern of TPP cubes on a glass slide, visualized with SRS imaging with contrast based on the CH vibrational modes in the 2800–3100 $cm^{-1}$ range. Scale bar is 100 μm. (B) SRS spectrum of the TPP cubes in the CH-stretching range *(red)* and the corresponding Raman spectrum *(black)*.

The TPP structures stand out clearly against the background. In Fig. 3.3.4B, the SRS signal intensity is plotted as a function of vibrational frequency in red. When the lasers are detuned to 2800 $cm^{-1}$, virtually no signal from the structures is observed, whereas the SRS signal is maximized near 2950 $cm^{-1}$. This vibrational energy corresponds to $CH_3$-stretching modes, which is an indicator of the density of methyl groups in the polymer. A second band, near 3050 $cm^{-1}$, is attributed to the CH vibration of the methine functional group (═CH—), and can be used as an indicator of carbon-carbon double bonds in the polymer structure. The Raman spectrum, measured on the same structure, is shown in black in Fig. 3.3.4B. It is clear that the SRS and Raman spectrum report the same vibrational information.

Fig. 3.3.5A shows an SEM image of two pyramids fabricated with TPP. These structures were made with acrylic resins that are rich in methylene groups. The CARS image in B is obtained by tuning the Raman shift to 2840 $cm^{-1}$, near the maximum of the methylene symmetric stretching vibration. In this example, narrowband (10 ps) pump and Stokes pulses were used. The 3D rendering is made possible by acquiring about 50 optically sectioned images at different depths. The CARS image reproduces the main features seen in the SEM image, down to a length scale of ~0.5 μm. The advantage is that the CARS image can, in principle, be obtained directly in situ on the TPP microfabrication unit, whereas the SEM image requires transportation of the specimen to a dedicated electron microscope.

Fig. 3.3.6A shows a CARS 3D rendering of another pyramid structure. Since the structure is fully digitized plane by plane, the 3D dataset can be inspected in various ways. Fig. 3.3.6B depicts a rendering, which allows an inspection of the bottom of the pyramid. This kind of information is difficult to obtain with electron microscopy, which is based on surface morphology and does not permit a closer look at the interior of the structure. This example thus shows that 3D optical imaging based on material density is a useful capability that goes beyond morphological mapping with SEM.

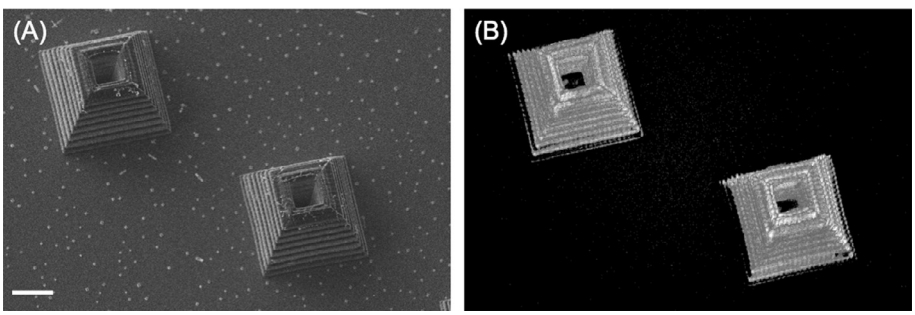


**Fig. 3.3.5** CARS density mapping based on C—H contrast at 2840 $cm^{-1}$. (A) SEM image of two pyramid structures. Scale bar is 20 μm. (B) 3D rendering of CARS images of the same structures.

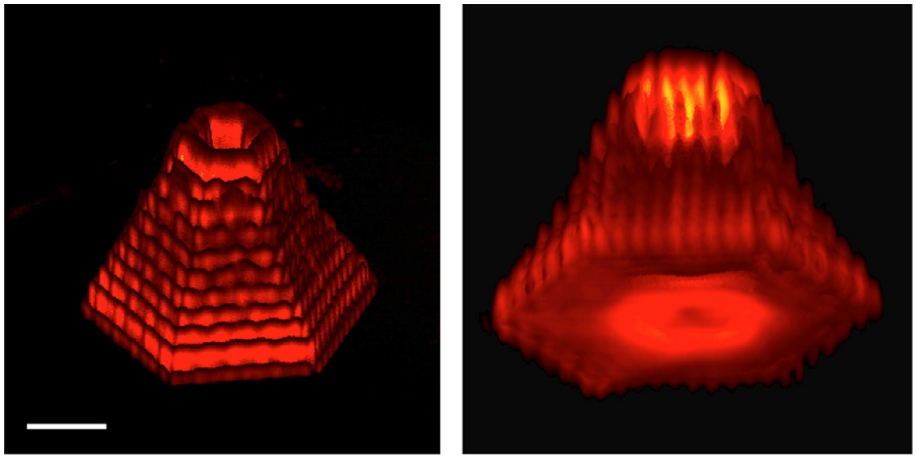


**Fig. 3.3.6** CARS density mapping based on C—H contrast at 2840 $cm^{-1}$. (A) 3D rendering of a pyramid structure. Scale bar is 10 µm. (B) Same structure, but with the structure digitally tilted, allowing a direct inspection of the bottom and interior of the structure.

## 4.2 Fingerprint contrast

The most useful property of CRS microscopy is that it enables imaging with contrast based on the density of certain chemical groups that play a role in the polymerization process. An example is shown in Fig. 3.3.7 In panel (A), the CARS fingerprint spectrum of a polymerized and a nonpolymerized resin is shown. This spectrum shows a lot of similarities with the Raman spectrum of Fig. 3.3.2, with prominent peaks near 1635 and 1720 $cm^{-1}$, the C═C and C═O stretching vibrations, respectively. Nonetheless, unlike the Raman spectrum, the CARS spectrum is dispersive. It floats on a nonresonant background and the peaks are slightly shifted toward lower wavenumbers. At the same time, a dip can be seen to the blue side of the peak. These features are well understood and are due to the interference between the resonant and the nonresonant contributions to the CARS signal [29]. At first sight, the dispersive line shape appears unattractive; however, the peak-dip difference provides additional contrast that can help discriminate polymerized from nonpolymerized materials.

Fig. 3.3.7B shows a CARS image of a TPP structure that spells out the word CARS. The structure is still surrounded by the (nonpolymerized) resin. Hence, this scenario mimics the visualization of a TPP structure in situ. The Raman shift is tuned to 1643 $cm^{-1}$, which is off-resonance and at the dip of the C═C stretching mode. For this setting, indicated by the red shaded area in panel (A), the signal from the nonpolymerized resin is very low, whereas the CARS signal of the polymerized material is slightly higher. Fig. 3.3.7B is normalized to the maximum signal, showing excellent contrast between the polymerized and nonpolymerized material. When the Raman shift is tuned to

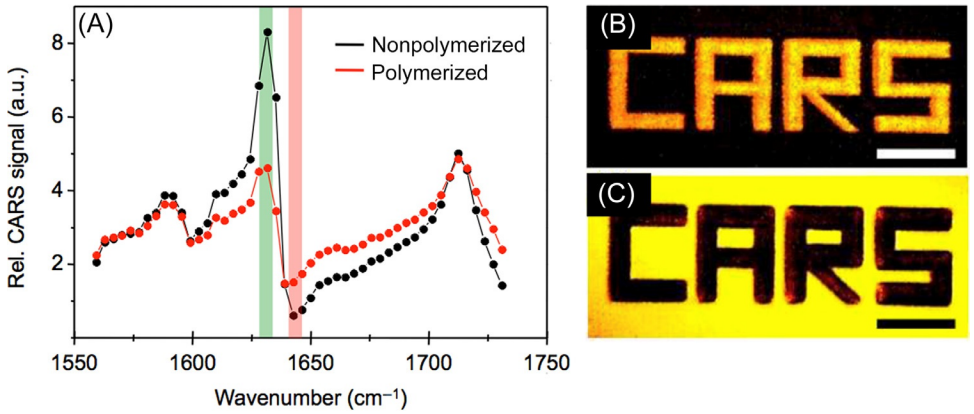


**Fig. 3.3.7** CARS spectral imaging of TPP structures. (A) CARS spectra of polymerized and nonpolymerized acrylic resins. The *green shaded area* is on-resonance with the C=C stretching mode, the *red shaded area* is off-resonance with the C=C mode. (B) Off-resonance CARS image at 1643 $cm^{-1}$ of a TPP structure that spells out the word CARS. (C) On-resonance image at 1628 $cm^{-1}$. Images have been rescaled for maximum contrast. Scale bar is 20 μm.

1628 $cm^{-1}$, on-resonance and near the peak of the C=C stretching mode, the contrast is reversed, as shown in Fig.3.3.7C. Now the strongest signal is obtained from the nonpolymerized material, whereas the polymerized material is significantly less. This example illustrates the usefulness of chemical imaging at certain settings of the Raman shift.

## 4.3 Degree of conversion

In the earlier example, the number density of the C=C modes is a direct measure of the amount of acrylic groups that have undergone polymerization. In Fig. 3.3.8A, CARS spectra are shown of TPP structures that have been written under identical conditions at different illumination powers. For higher illumination powers, we expect a higher degree of conversion, and thus a more significant decrease in the number of C=C groups. This is indeed observed. The CARS signal at 1628 $cm^{-1}$, on resonance with the C=C vibrational mode, is decreasing when the illumination power is raised.

Since the CARS is not linear with the number Raman scatterers, the information in panel 8(A) is not a direct quantitative account of the number of C=C bonds in the sample. It is possible to extract the vibrationally resonant information from the CARS spectrum by applying a phase retrieval algorithm. There are several of such algorithms that have proven reliable, among which are the maximum entropy method (MEM) and the modified Kramers-Kronig method [30]. In Fig. 3.3.8B, the retrieved Raman spectrum is shown after phase retrieval with the MEM. Because the Raman spectrum scales linearly with the number of vibrational oscillators, the intensity of the C=C resonance is now directly proportional to the number of C=C bonds.

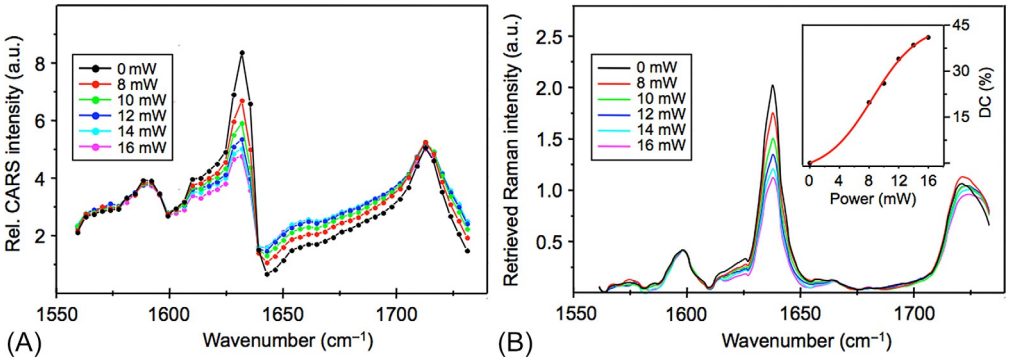


**Fig. 3.3.8** (A) CARS fingerprint spectra of TPP structures fabricated under identical conditions but with different illumination powers. (B) Retrieved Raman spectra after application of the maximum entropy method for phase retrieval. The inset shows the degree of conversion (DC) as a function of laser illumination power.

The degree of conversion can now be computed. It is useful to ratio the C═C Raman signal to an internal reference. In this case, the 1595 $cm^{-1}$ resonance of the photoinitiator is a good choice for the internal reference, since this resonance is unaffected by the polymerization process. However, this peak is not universal, as it depends on the use of photoinitiator. In general, it is helpful to use an internal reference that is independent of the photoinitiator. The C═O resonance is a reasonable choice. Even though the C═O Raman resonance may shift and change in amplitude before and after polymerization, these changes are relatively small, as is evident from Fig. 3.3.8B. With these assumptions in mind, we may define the percentage of the degree of conversion (DC) as follows:

$$\mathrm{DC} = \left[1 - \frac{A_{\mathrm{C=C}}/A_{\mathrm{C=O}}}{A'_{\mathrm{C=C}}/A'_{\mathrm{C=O}}}\right] \times 100$$

where the integrated intensities of the Raman resonance before polymerization are indicated as $A'_{\mathrm{C=C}}$ and $A'_{\mathrm{C=O}}$, and after polymerization as $A_{\mathrm{C=C}}$ and $A_{\mathrm{C=O}}$. A plot of the DC, based on the data in Fig. 3.3.8B, is shown in the inset. The sigmoidal dependence of the DC with laser power is consistent with established models of polymerization of highly branched acrylic monomers [31]. This example underlines that CRS imaging allows a direct recording of DC, with the possibility to retrieve such information in situ with submicrometer resolution.

## 4.4 Comparison with spontaneous Raman scattering

As emphasized in the chapter, the most important advantage of CRS microscopy over the conventional Raman microscope is the much-improved image acquisition time. To make this more explicit in the context of TPP structure imaging, Fig. 3.3.9 shows a

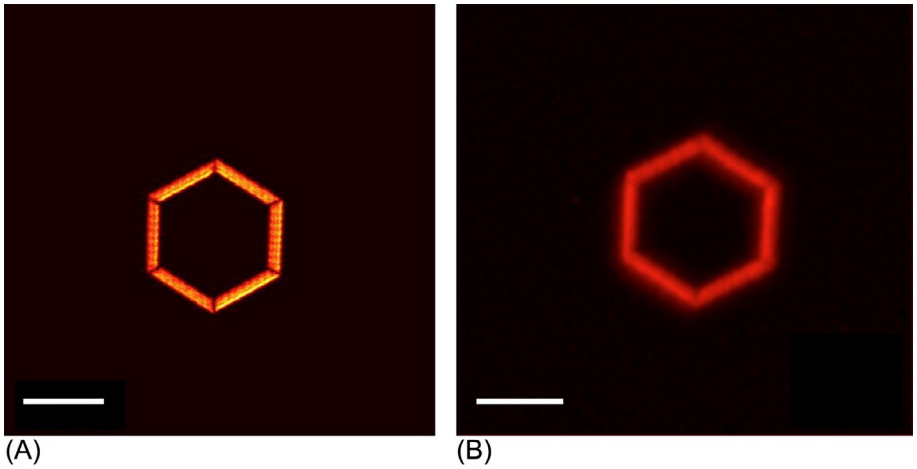


**Fig. 3.3.9** Comparison between the imaging speed of CARS and Raman microscopy. A hexagon TPP structure is visualized in a CARS microscope (A), with an image acquisition time of 1 s, and in a Raman microscope (B), with an image acquisition time of 5 h. Scale bars are 20 μm.

comparison between CARS microscopy and Raman microscopy when visualizing the same TPP structure. The CARS image, shown in panel 3.3.9A, was taken with an 800-nm pump beam and a 1050-nm Stokes beam, both derived from a femtosecond light source. Under these conditions, the structure is visualized based on the density of CH vibrational oscillators. The average power was 4 mW for the pump and 10 mW for the Stokes. Using a 1.1-NA objective lens, a 512 × 512-pixel image was acquired from the hexagon TPP structure within 1 s. The structure is clearly visible under these conditions.

By contrast, the Raman image was taken by using a 514.5-nm laser light source at total average power of 35 mW. A 0.75-NA objective lens was used, and the image contains 14K pixels, with a total acquisition time of 5 h. Although the structure is clearly imaged, the acquisition time is more than four orders of magnitude longer. Even though the CARS and Raman images are obtained under slightly different conditions, it is evident that the CRS approach offers chemical imaging of TPP structures at imaging speeds that are orders of magnitude higher than what can be acquired on a conventional Raman microscope. In the next section, we will discuss a particular application enabled by CRS that goes much beyond what can be achieved with Raman microscopy.

## 5 Following polymerization during TPP fabrication

The earlier examples illustrate that CRS microscopy can provide useful information about TPP structures before and after polymerization. In principle, the imaging speed of CRS is fast enough for measuring TPP structures during the writing process. The ability to see the TPP structure during laser writing can be particularly useful. For instance,

the shrinking and/or swelling of polymerized material immediately after illumination is an important factor that defines the material property of the eventual structure. Controlling such parameters during writing, by revisiting areas of lower quality, can be important. More generally, direct in situ visualization provides a direct link between the structure and the laser writing pattern. Since there are multiple laser writing patterns that can be pursued to attain a desired end result, on-the-spot inspection can help identify the best scanning patterns to achieve a given structure.

An example of the capability of in situ imaging during laser writing is shown in Fig. 3.3.10 [10]. Here the structure is written in an acrylic resin with a fixed laser beam

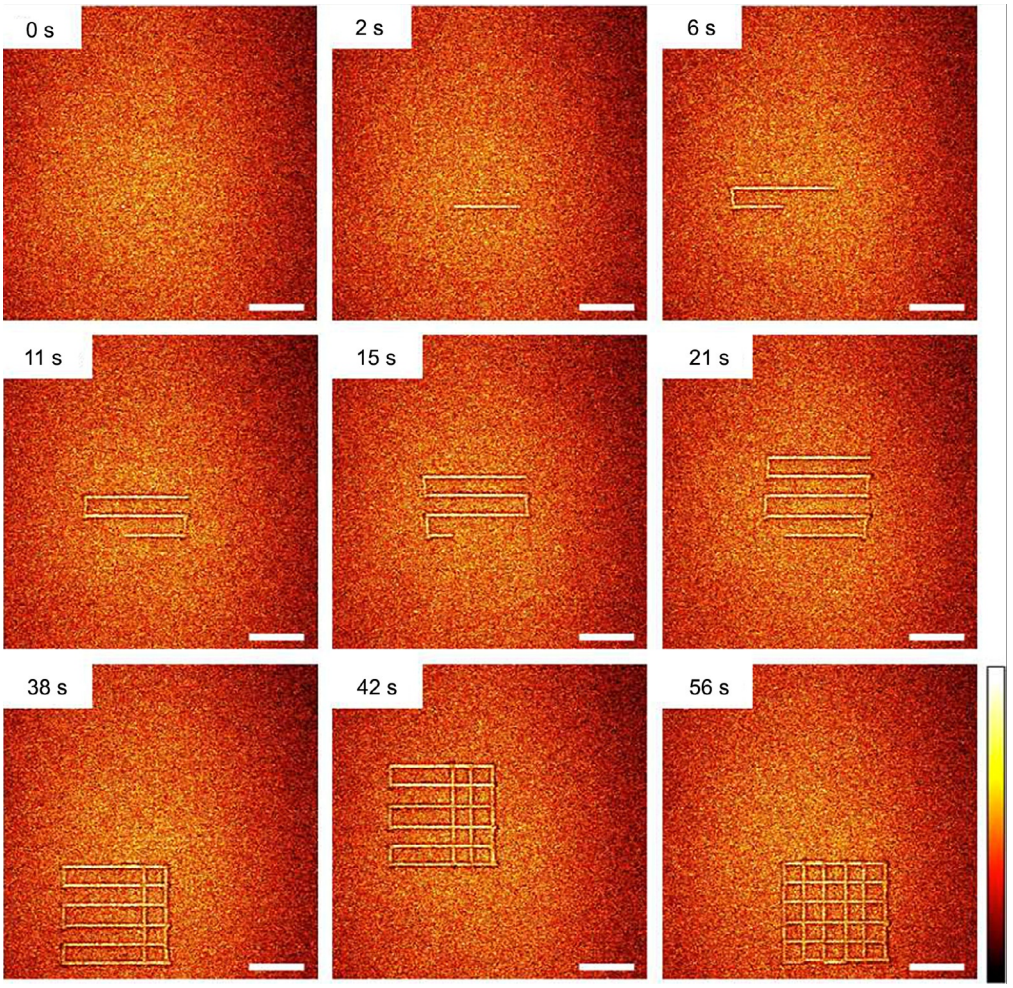


**Fig. 3.3.10** Direct CRS visualization of TPP structures in situ during laser writing. The images are taken at different times during the writing of a two-dimensional microstructure. Scale bar is 25 μm.

by movement of the stage, while CARS imaging is conducted through galvanometric laser scanning with an additional pair of pump and Stokes beams. The system is based on a single near-infrared femtosecond light source with a center wavelength near 800 nm. Part of the laser beam is used for TPP structure fabrication, while another portion of the laser power is used to produce the pump and Stokes beam for CARS imaging. The pump beam consists of the 800-nm pulses, while the Stokes beam is generated through supercontinuum generation. This broadband configuration allows excitation of the entire C—H stretching band at once, enabling rapid imaging based on the density of C—H groups in the material. Since the density of the polymerized material is markedly different from the nonpolymerized material, the C—H signal provides sufficient contrast for discriminating the TPP structure from the nonpolymerized resin.

The two-dimensional TPP structure shown in Fig. 3.3.10 can be clearly identified during the writing process. At a frame rate of 2 images per second, the fabrication process can be followed on a timescale sufficient to identify crucial features. The example also illustrates that CRS imaging can be performed under conditions that do not perturb the writing of TPP structures. At a pixel dwell time on the microsecond scale, the peak powers of the pump and Stokes beams are sufficiently low so as not to trigger polymerization in the resin.

Although this example underlines the usefulness of CRS imaging in TPP fabrication, there is room to further exploit the chemical sensitivity of the technique. By tuning to the fingerprint region, as discussed earlier, a direct metric of the degree of polymerization can be obtained. It is attractive to perform CRS imaging based on such metrics during laser writing, which would provide critical information about structure quality in situ.

## 6 Conclusion and outlook

In this chapter, we have discussed the utility of CRS microscopy for the inspection and characterization of TPP structures. The examples shown emphasize that meaningful chemical information can be obtained with CRS imaging, including material density as defined through the density of C—H chemical groups and the degree of conversion. Such information is difficult to acquire with other techniques, especially in situ. Nonetheless, despite these attractive features, the CRS technique requires that a dedicated light source, laser scanner, and suitable detectors be incorporated into the TPP fabrication platform. Although feasible, such modifications are currently nonstandard and rather expensive. In this regard, the smart use of a femtosecond light source for both TPP structure fabrication and CRS visualization would facilitate the use of coherent Raman technology for this purpose. Recent progress in laser light sources and light management makes it possible to not only implement more compact solutions, but also to devise excitation schemes that maximally use the chemical sensitivity of CRS. It can be expected that

technical developments along these lines will make the CRS implementation simpler and more reliable, thus improving their utility for TPP structure writing.

## References


[1] N.C. LaFratta, T. Baldacchini, Two-photon polymerization metrology: characterization methods of mechanisms and microstructures, Micromachines 8 (2017) 101.
[2] N. Silikas, G. Eliades, D.C. Watts, Light intensity effects on resin-composite degree of conversion and shrinkage strain, Dent. Mater. 16 (2000) 292–296.
[3] L.E. Silva Soares, A.A. Martin, A.L. Barbosa Pinheiro, Degree of conversion of composite resin: a Raman study, J. Clin. Laser Med. Surg. 21 (2003) 357–362.
[4] L.J. Jiang, Y.S. Zhou, W. Xiong, Y. Gao, X. Huang, L. Jiang, T. Baldacchini, J.-F. Silvain, Y.F. Lu, Two-photon polymerization: investigation of chemical and mechanical properties of resins using Raman microspectroscopy, Opt. Lett. 39 (2014) 3034–3037.
[5] F. Burmeister, S. Steenhusen, R. Houbertz, U.D. Zeitner, S. Nolte, A. Tünnermann, Materials and technologies for fabrication of three-dimensional microstructures with sub-100 nm feature sizes by two-photon polymerization, J. Laser Appl. 24 (2012) 042014.
[6] G. Turrell, J. Corset, Raman Microscopy, Elsevier, San Diego, CA, 1996.
[7] C.L. Evans, X.S. Xie, Coherent anti-Stokes Raman scattering microscopy: chemical imaging for biology and medicine, Annu. Rev. Anal. Chem. 1 (2008) 883–909.
[8] J.L. Suhalim, J.C. Boik, B.J. Tromberg, E.O. Potma, The need for speed, J. Biophotonics 5 (2012) 387–395.
[9] J.-X. Cheng, X.S. Xie, Coherent Raman Scattering Microscopy, CRC Press, Boca Raton, FL, 2013.
[10] T. Baldacchini, R. Zadoyan, In situ and real time monitoring of two-photon polymerization using broadband coherent anti-Stokes Raman scattering microscopy, Opt. Express 18 (2010) 19219–19231.
[11] T. Baldacchini, M. Zimmerley, C.-H. Kuo, E.O. Potma, R. Zadoyan, Characterization of microstructures fabricated by two-photon polymerization using coherent anti-Stokes Raman scattering microscopy, J. Phys. Chem. B 113 (2009) 12663–12668.
[12] G. Placzek, Rayleigh Streuung und Raman-Effeckt, in: E. Marx (Ed.), Handbuch der Radiologie, Academische-Verlag, Leipzig, 1934.
[13] R.C. Prince, R.R. Frontiera, E.O. Potma, Stimulated Raman scattering: from bulk to nano, Chem. Rev. 117 (2017) 5070–5094.
[14] C.W. Freudiger, W. Min, B.G. Saar, S. Lu, G.R. Holtom, C. He, J.C. Tsai, J.X. Kang, X.S. Xie, Label-free biomedical imaging with high sensitivity by stimulated Raman scattering microscopy, Science 322 (2008) 1857.
[15] E. Ploetz, S. Laimgruber, S. Berner, W. Zinth, P. Gilch, Femtosecond stimulated Raman microscopy, Appl. Phys. B Lasers Opt. 87 (2007) 389–393.
[16] P. Nandakumar, A. Kovalev, A. Volkmer, Vibrational imaging based on stimulated Raman scattering microscopy, New J. Phys. 11 (2009) 033026.
[17] D. Kim, D.S. Choi, J. Kwon, S.-H. Shim, H. Rhee, M. Cho, Selective suppression of stimulated Raman scattering with another competing stimulated Raman scattering, J. Phys. Chem. Lett. 8 (2017) 6118–6123.
[18] H. Kim, G.W. Bryant, S.J. Stranick, Superresolution four-wave mixing microscopy, Opt. Express 20 (2012) 6042–6051.
[19] W.R. Silva, C.T. Graefe, R.R. Frontiera, Toward label-free super-resolution microscopy, ACS Photonics 3 (2016) 79–86.
[20] A.-G. Alba, M. Richa, L. Eun Seong, O.P. Eric, Biological imaging with coherent Raman scattering microscopy: a tutorial, J. Biomed. Opt. 19 (2014) 071407.
[21] J.-X. Cheng, A. Volkmer, L.D. Book, X.S. Xie, An epi-detected coherent anti-Stokes Raman scattering (E-CARS) microscope with high spectral resolution and high sensitivity, J. Phys. Chem. B 105 (2001) 1277–1280.

[22] M. Müller, J.M. Schins, Imaging the thermodynamic state of lipid membranes with multiplex CARS microscopy, J. Phys. Chem. B 106 (2002) 3715–3723.
[23] S.H. Parekh, Y.J. Lee, K.A. Aamer, M.T. Cicerone, Label-free cellular imaging by broadband coherent anti-Stokes Raman scattering microscopy, Biophys. J. 99 (2010) 2695–2704.
[24] T. Hellerer, A.M.K. Enejder, A. Zumbusch, Spectral focusing: high spectral resolution spectroscopy with broad-bandwidth laser pulses, Appl. Phys. Lett. 85 (2004) 25–27.
[25] E.R. Andresen, P. Berto, H. Rigneault, Stimulated Raman scattering microscopy by spectral focusing and fiber-generated soliton as Stokes pulse, Opt. Lett. 36 (2011) 2387–2389.
[26] X. Nan, E.O. Potma, X.S. Xie, Nonperturbative chemical imaging of organelle transport in living cells with coherent anti-Stokes Raman scattering microscopy, Biophys. J. 91 (2006) 728–735.
[27] C.-S. Liao, M.N. Slipchenko, P. Wang, J. Li, S.-Y. Lee, R.A. Oglesbee, J.-X. Cheng, Microsecond scale vibrational spectroscopic imaging by multiplex stimulated Raman scattering microscopy, Light-Sci. Appl. 4 (2015) e265.
[28] P. Kunwar, J. Toivonen, M. Kauranen, G. Bautista, Third-harmonic generation imaging of three-dimensional microstructures fabricated by photopolymerization, Opt. Express 24 (2016) 9353–9358.
[29] G.L. Eesley, Coherent Raman Spectroscopy, Pergamon Press, Oxford, 1981.
[30] M.T. Cicerone, K.A. Aamer, Y.J. Lee, E. Vartiainen, Maximum entropy and time-domain Kramers–Kronig phase retrieval approaches are functionally equivalent for CARS microspectroscopy, J. Raman Spectrosc. 43 (2012) 637–643.
[31] E. Selli, I.R. Bellobono, Photopolymerization of multifunctional monomers: kinetic aspects, in: J.P. Fouassier, J.F. Rabek (Eds.), Radiation Curing in Polymer and Technology, Elsevier, New York, 1993, pp. 1–32.